

Supplementary Information

# Ag<sub>2</sub>Cu<sub>2</sub>O<sub>3</sub> - a catalyst template material for selective electroreduction of CO to C<sub>2+</sub> products

Nemanja Martić<sup>1</sup>, Christian Reller<sup>1</sup>, Chandra Macauley<sup>2</sup>, Mario Löffler<sup>3,4</sup>, Andreas M. Reichert<sup>3,4</sup>, Thomas Reichbauer<sup>1</sup>, Kim-Marie Vetter<sup>1</sup>, Bernhard Schmid<sup>1</sup>, David McLaughlin<sup>3,4</sup>, Paul Leidinger<sup>5</sup>, David Reinisch<sup>1</sup>, Christoph Vogl<sup>1</sup>, Karl J. J. Mayrhofer<sup>3,4</sup>, Ioannis Katsounaros<sup>3</sup>, and Günter Schmid<sup>1\*</sup>

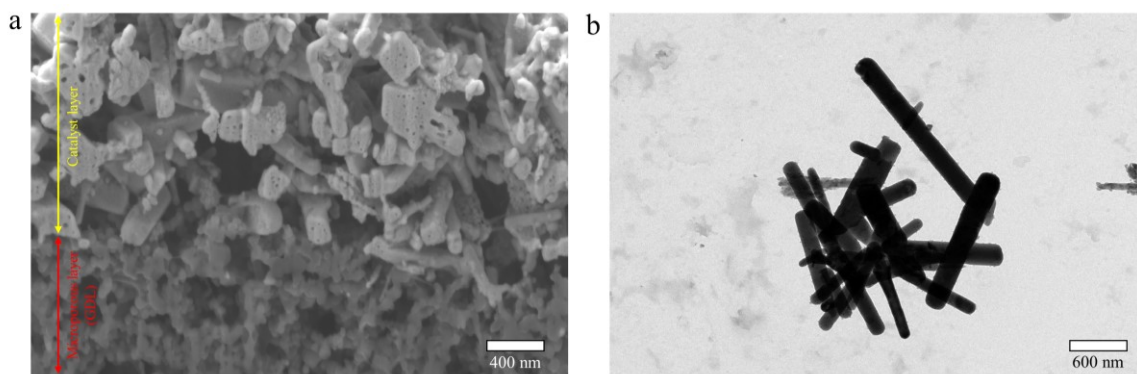
N. Martić, Dr. C. Reller, T. Reichbauer, K.M. Vetter, B. Schmid, D. Reinisch, C. Vogl, Dr. G. Schmid  
Siemens Gas and Power GmbH & Co. KG, SE NEB TP COS  
Günther-Scharowsky-Str. 1  
91058 Erlangen, Germany  
E-mail: guenter.schimd@siemens.com

Dr. C. Macauley  
Department of Materials Science & Engineering  
Friedrich-Alexander-Universität Erlangen-Nürnberg (FAU)  
Cauerstr. 5  
91058 Erlangen, Germany

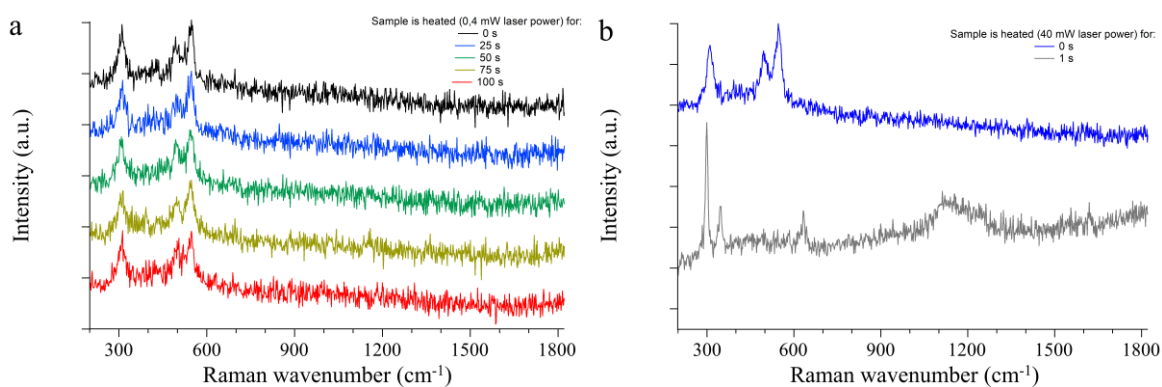
M. Löffler, A. M. Reichert, D. McLaughlin, Prof. Dr. K. J. J. Mayrhofer, Dr. I. Katsounaros  
Helmholtz Institute Erlangen-Nürnberg for Renewable Energy (IEK-11)  
Forschungszentrum Jülich GmbH  
Egerlandstr. 3  
91058 Erlangen, Germany

M. Löffler, A. M. Reichert, D. McLaughlin, Prof. Dr. K. J. J. Mayrhofer  
Department of Chemical and Biological Engineering  
Friedrich-Alexander-Universität Erlangen-Nürnberg (FAU)  
Immerwahrstr. 2a  
91058 Erlangen, Germany

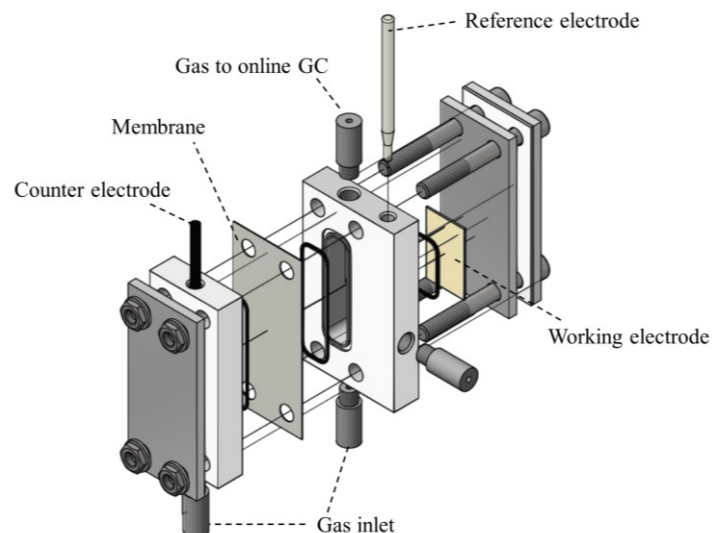
Paul Leidinger  
Catalysis Research Center  
Technical University of Munich (TUM)  
Ernst-Otto-Fischer-Str. 1  
85748 Garching, Germany



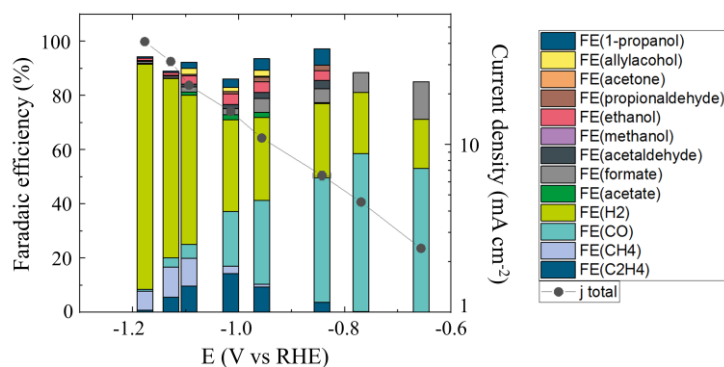
**Supplementary Figure 1.** (a) SEM image showing a cross-section of a Gas Diffusion Layer (GDL) coated with pristine  $\text{Ag}_2\text{Cu}_2\text{O}_3$  particles. Focused ion beam (FIB) was used to mill away a part of the sample to obtain the cross-section which exposed a closed, inner-porous structure of  $\text{Ag}_2\text{Cu}_2\text{O}_3$  particles. (b) TEM image of  $\text{Ag}_2\text{Cu}_2\text{O}_3$  particles.



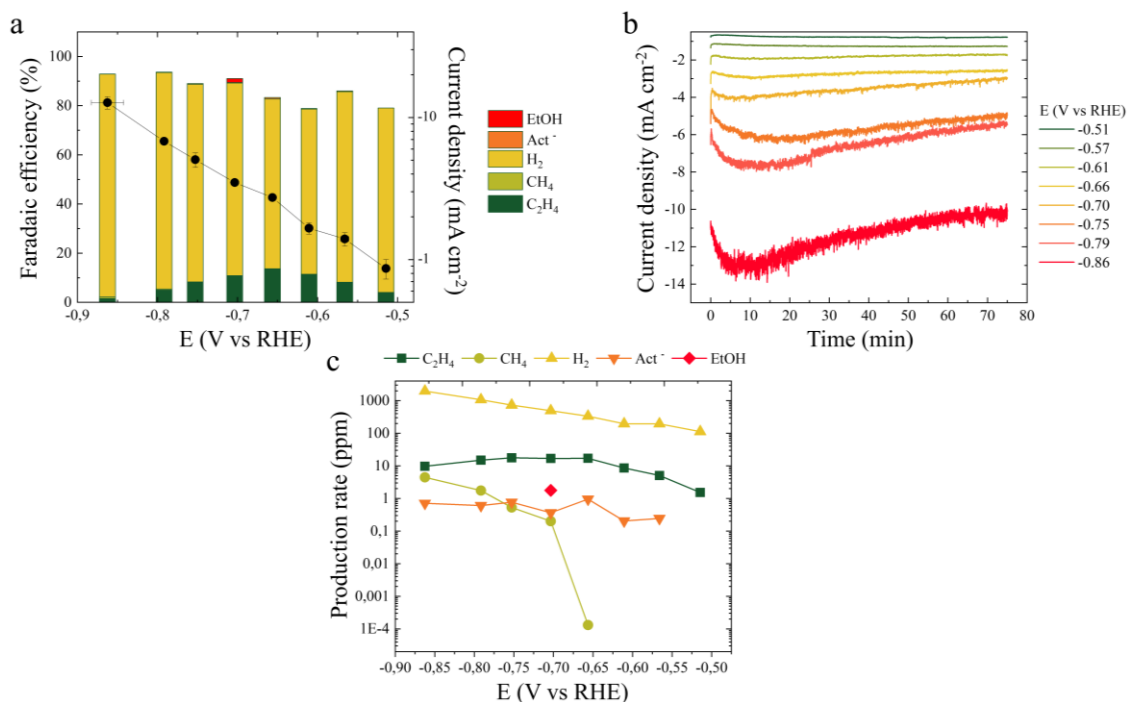
**Supplementary Figure 2.** (a) Five Raman spectra acquired consecutively at the same position in steps of 25 s with 5x5 s acquisition time and laser power of 0.4 mW. No change in signal ratio or intensity was detected and no additional peaks appeared in the spectra which led us to the conclusion that there was no structural degradation of the  $\text{Ag}_2\text{Cu}_2\text{O}_3$  phase. (b) Spectra of the  $\text{Ag}_2\text{Cu}_2\text{O}_3$  powder acquired before (blue) and after (gray) laser induced heating of the sample for 1 s with 40 mW laser power. Exposure of the sample to 40 mW laser power led to degradation of the material and the loss of all signals previously assigned to  $\text{Ag}_2\text{Cu}_2\text{O}_3$ . New signals belonging to copper(II) oxide (CuO) at approx.  $300\text{ cm}^{-1}$ ,  $349\text{ cm}^{-1}$  and  $634\text{ cm}^{-1}$  are identified<sup>1</sup>. The broad peak between  $1000\text{--}1300\text{ cm}^{-1}$  was found to belong to a second order scattering effect of the CuO<sup>2</sup>. The spectra are normalized for better illustration.



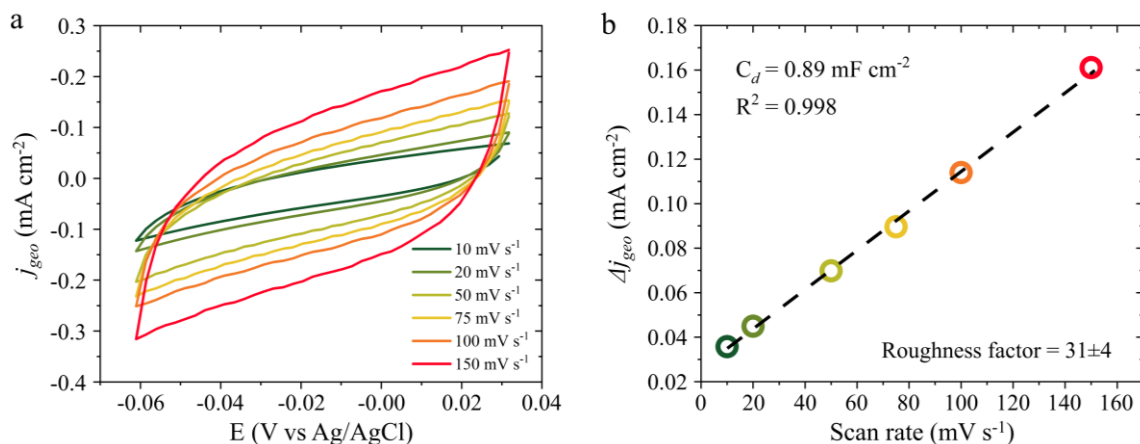
**Supplementary Figure 3.** Exploded-view schematic of a two-compartment electrolysis cell utilized for low current density studies. The compartments were filled with CO<sub>2</sub>-saturated 0.05 M K<sub>2</sub>CO<sub>3</sub> electrolyte. CO<sub>2</sub> was constantly purged through the electrolyte at 30 sccm during the electrolysis experiments. The compartments were separated by a membrane (Fumasep BPM). A three-electrode set-up with Ag/AgCl as reference electrode, Ir-MMO plate as counter electrode and a catalyst-coated glassy carbon plate as working electrode was used. The exit gas stream from the cathode compartment was directly coupled with a gas chromatograph. The data collected vs. Ag/AgCl reference were converted to a reversible hydrogen electrode (RHE) scale.



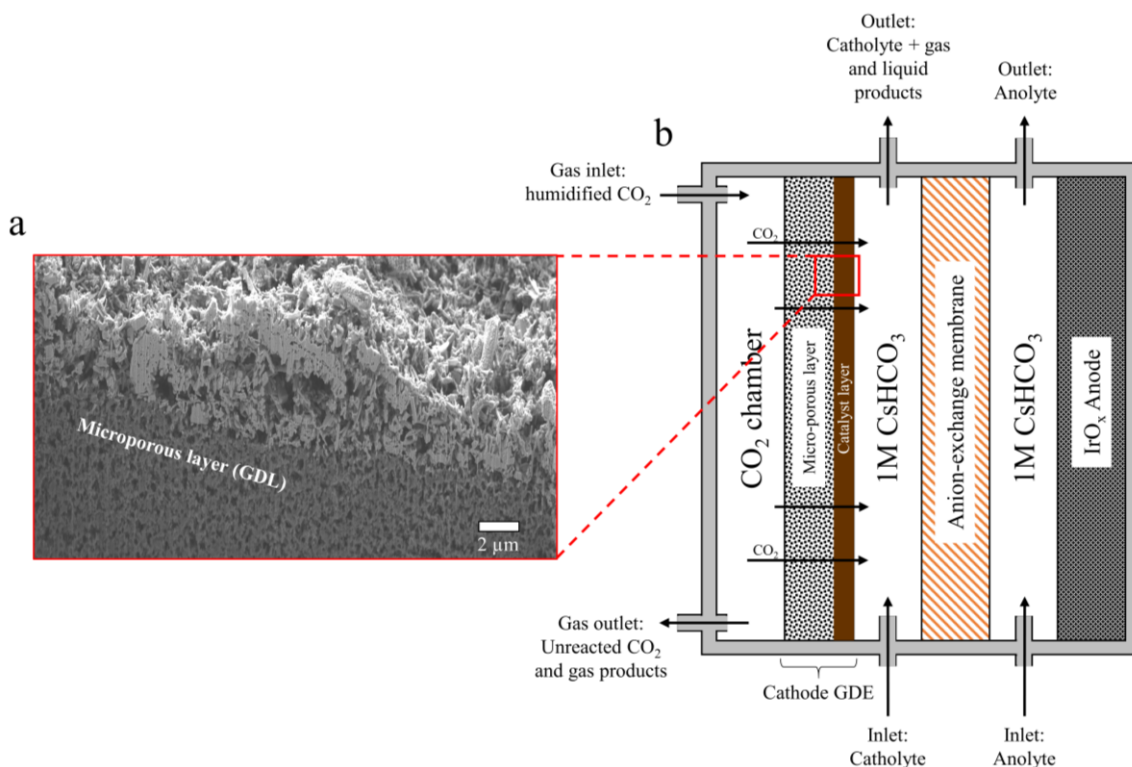
**Supplementary Figure 4.** Faradaic efficiencies for H<sub>2</sub> and all detected CO<sub>2</sub>RR products as a function of the potential measured at the cathode.



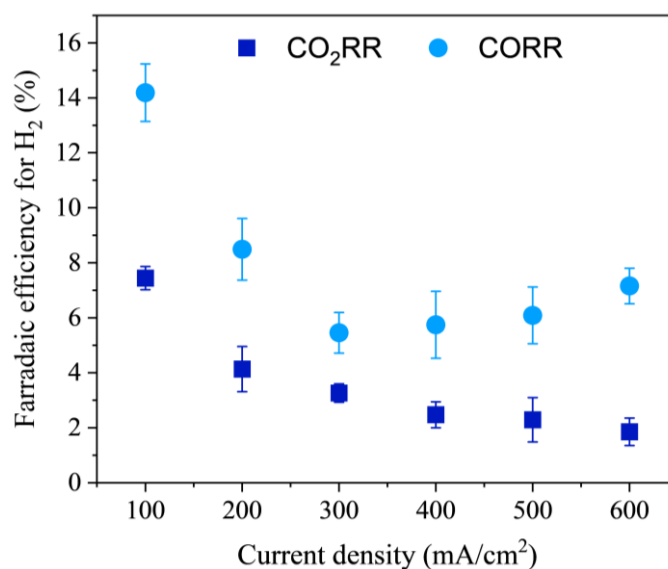
**Supplementary Figure 5.** (a) Faradaic efficiency for all detected CORR products and H<sub>2</sub> as a function of the potential measured at the cathode. (b) Current density measured for 8 different potential as a function of time. (c) Production rates calculated in ppm for detected CORR products and H<sub>2</sub> as a function of the potential measured at the cathode.



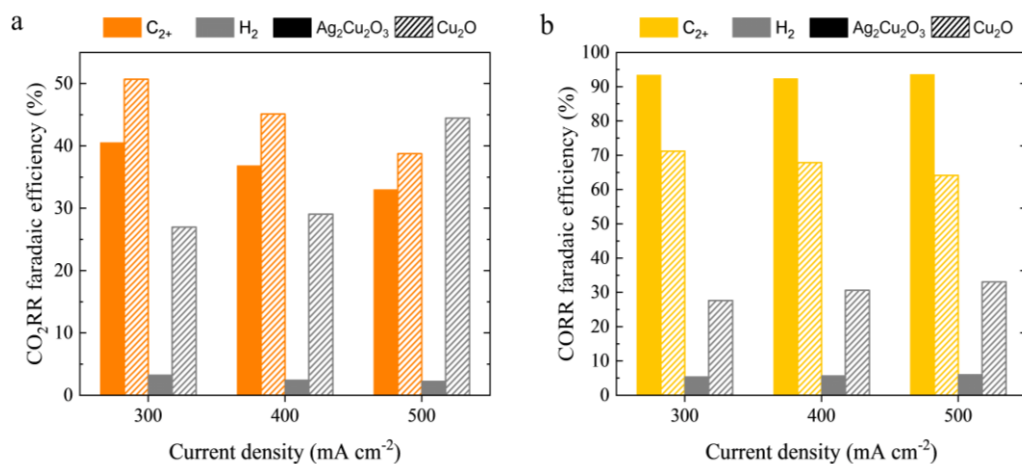
**Supplementary Figure 6.** Electrochemical surface area measurement (ECSA). (a) The double layer-capacitance was estimated by measuring CVs with different scan rates in the potential range between -0.06 and 0.03 V vs Ag/AgCl where no Faradaic processes occurred. 0.1M KHCO<sub>3</sub> solution saturated with Ar was used as electrolyte. (b) Average charging current density was plotted against the scan rate and the  $C_{dl}$  was obtained from the slope. For estimating the roughness factor, a double-layer capacitance of a smooth Cu surface was taken to be 29  $\mu\text{F cm}^{-1}$ , based on previous measurements<sup>3</sup>.



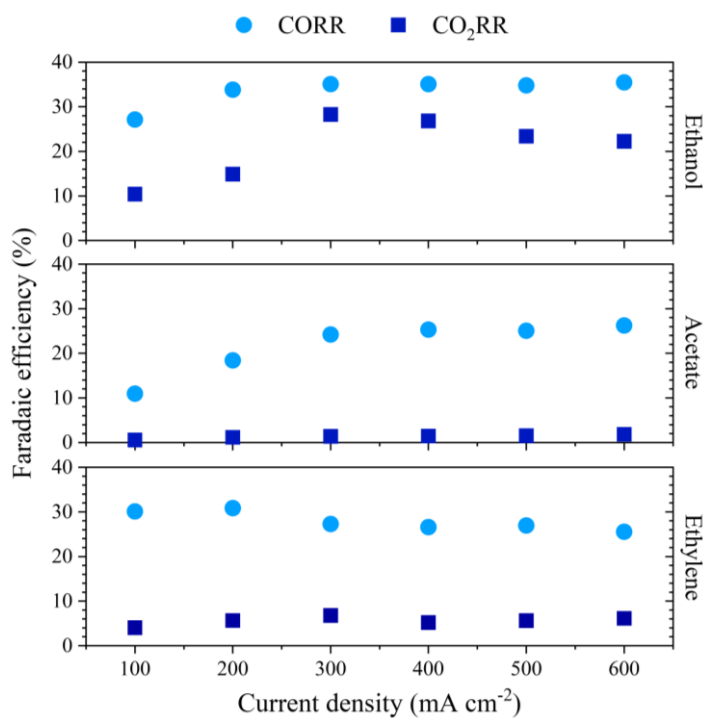
**Supplementary Figure 7.** (a) SEM image showing a cross section belonging to a typical GDE used for electrochemical characterization of  $\text{Ag}_2\text{Cu}_2\text{O}_3$ . (b) Schematic representation of a flow cell used for amperostatic, high current density experiments. A three-electrode set-up with  $\text{Ag}/\text{AgCl}$  as reference electrode,  $\text{Ir-MMO}$  plate as counter electrode and a  $\text{Ag}_2\text{Cu}_2\text{O}_3$ -coated GDL ( $2\text{ cm}^2$ ) fitted inside of a titanium frame as working electrode was used. The reference electrode was placed outside of the cell, in close proximity of the catholyte inlet. Anion exchange membrane (Fumasep, FAB-PK-130) was used to separate the catholyte and anolyte flows. During operation, 100 mL of catholyte (1M  $\text{CsHCO}_3$ ) and 100 mL of anolyte (1M  $\text{CsHCO}_3$ ) were continuously circulated ( $30\text{ mL min}^{-1}$ ) through the cell during operation.



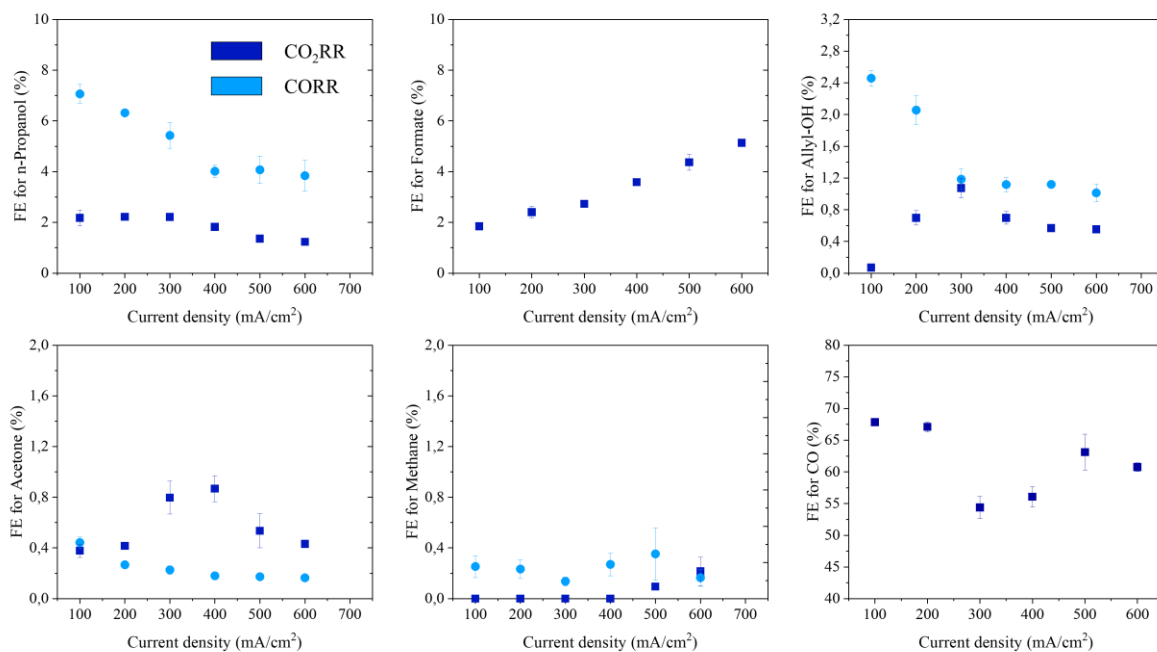
**Supplementary Figure 8.** Faradaic efficiency for hydrogen obtained for  $\text{CO}_2\text{RR}$  and  $\text{CORR}$  plotted as a function of current density for experiments performed in a flow cell reactor.



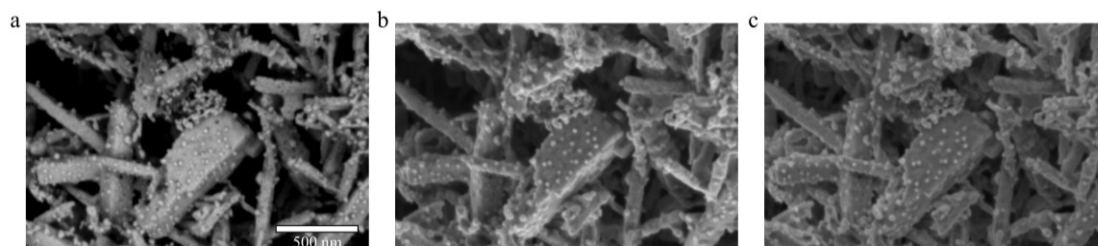
**Supplementary Figure 9.** Faradaic efficiencies for C<sub>2+</sub> products and hydrogen, when Ag<sub>2</sub>Cu<sub>2</sub>O<sub>3</sub> and Cu<sub>2</sub>O are used as initial catalyst materials, are used plotted against current density for both (a) CO<sub>2</sub>RR and (b) CORR. Cu<sub>2</sub>O reference powder bought from Sigma Aldrich (<7 μm, 97%) was used. The Cu<sub>2</sub>O GDEs were manufactured following the same procedure as described for Ag<sub>2</sub>Cu<sub>2</sub>O<sub>3</sub> GDEs in the Methods section of the main text.



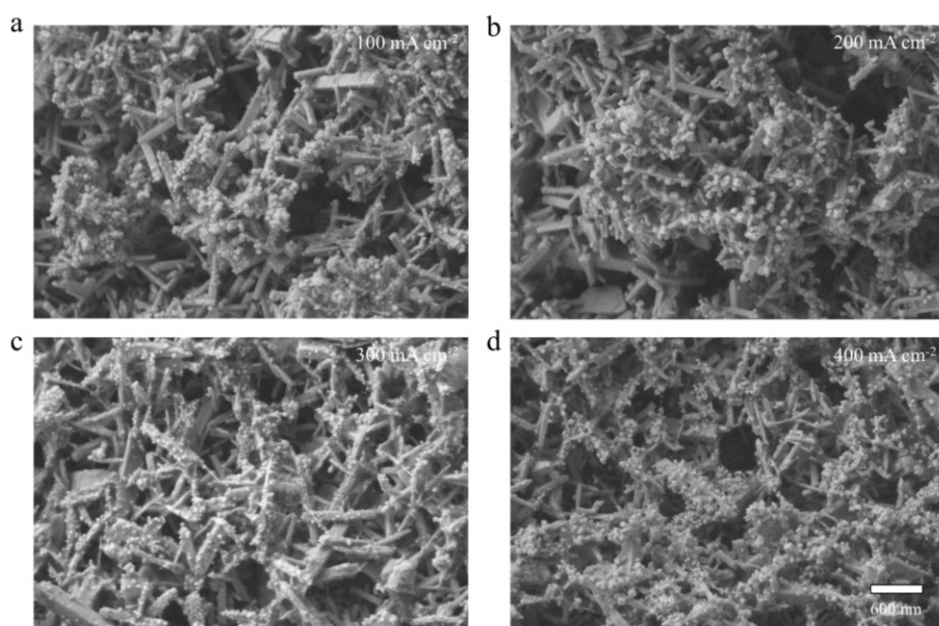
**Supplementary Figure 10.** Faradaic efficiencies for ethanol, ethylene and acetate plotted against current density for both CO<sub>2</sub>RR and CORR.



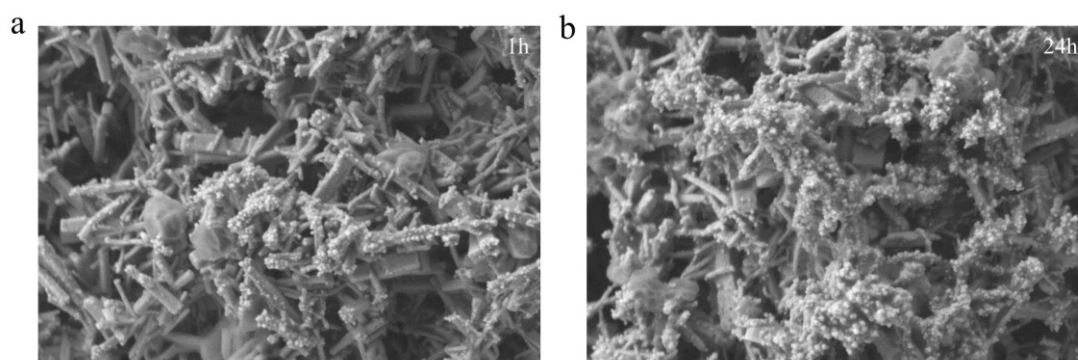
**Supplementary Figure 11.** Faradaic efficiency belonging to CO<sub>2</sub>RR and CORR products plotted as a function of current density. Methanol was only detected in traces (less than 0.1% FE at all tested current densities).



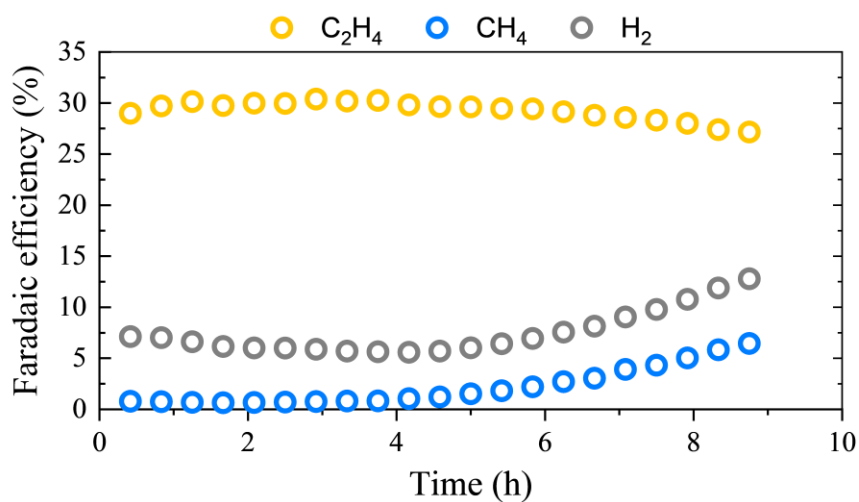
**Supplementary Figure 12.** SEM images using different SEM detectors.



**Supplementary Figure 13.** SEM images of post-electrolysis GDEs tested at (a) 100 mA cm<sup>-2</sup>, (b) 200 mA cm<sup>-2</sup>, (c) 300 mA cm<sup>-2</sup> and (d) 400 mA cm<sup>-2</sup>. The scale bar for all SEM images is 600 nm.

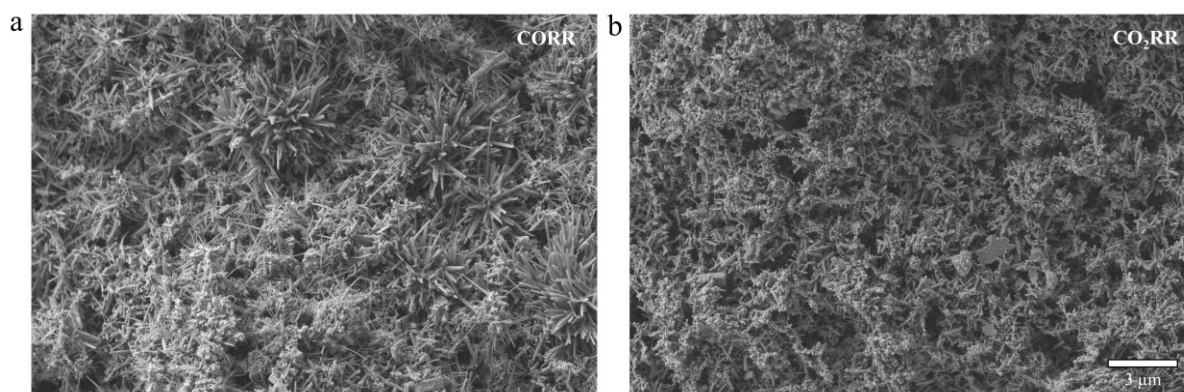


**Supplementary Figure 14.** SEM images of post-electrolysis GDEs tested at a constant current density of 300 mA cm<sup>-2</sup> for (a) 1h and (b) 24h.

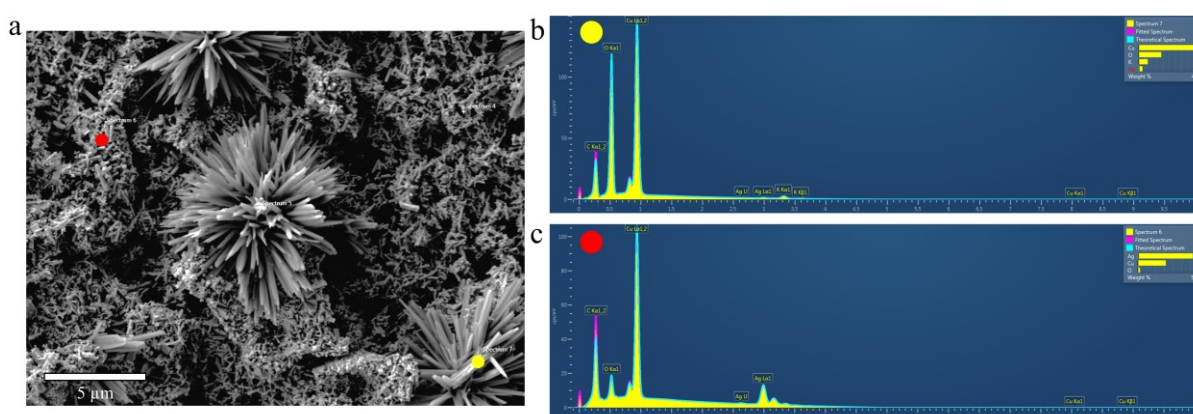


**Supplementary Figure 15.** CORR gas product selectivity during long-term stability test in 1M CsHCO<sub>3</sub> at a constant current density of 300 mA cm<sup>-2</sup>. All experimental conditions were kept identical to the ones

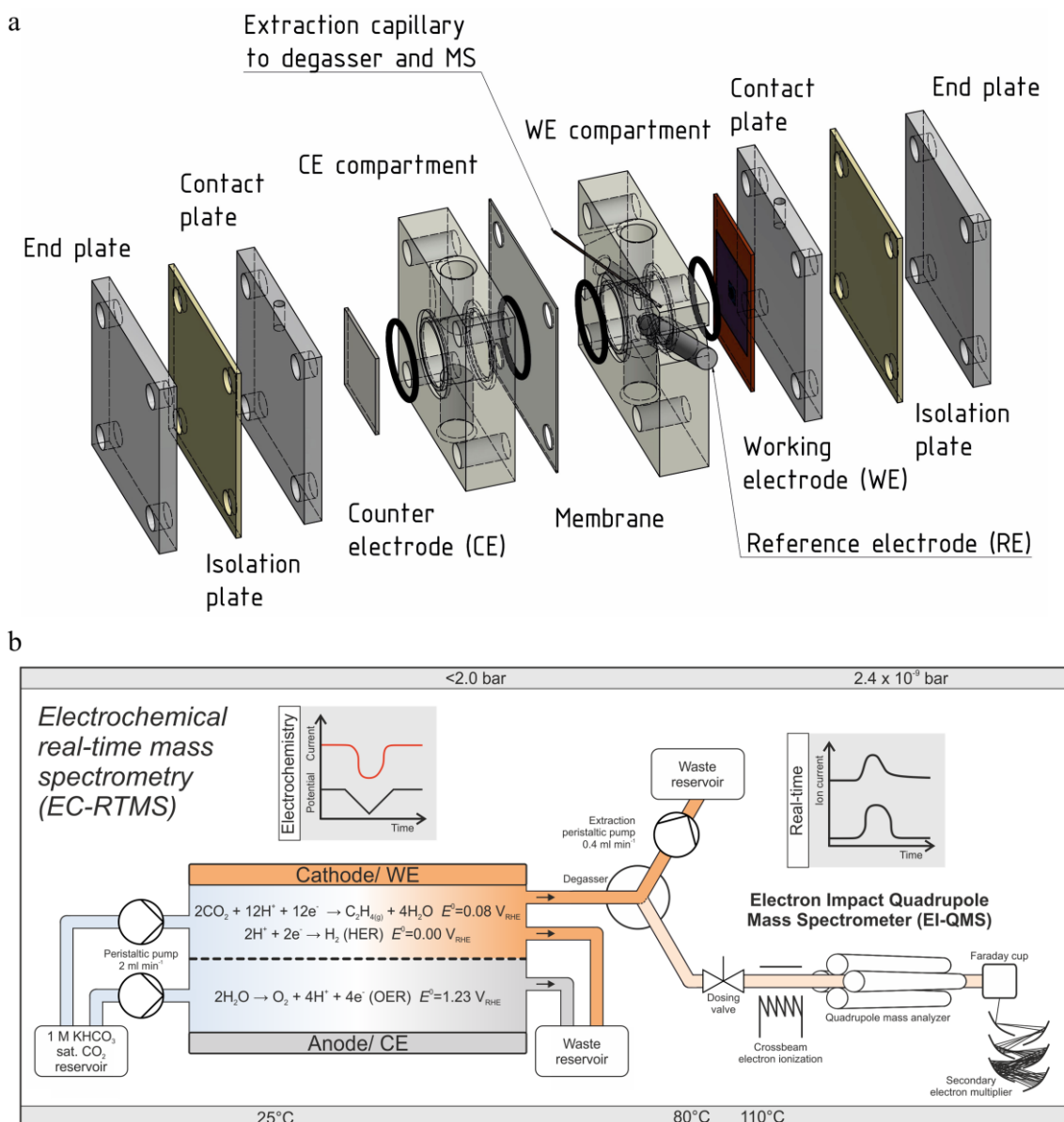
used for CO<sub>2</sub>RR long-term stability testing showed in Figure 3e of the main text. In order to investigate the observed decrease in stability compared to CO<sub>2</sub>RR, post-electrolysis microscopy and EDX analysis of the electrodes have been performed (Supplementary Fig. 15). The obtained images showed that the electrode's surface was uniformly covered with urchin-like agglomerates whose size ranged from 3 to 10 μm. Additionally, smaller and much finer needle-like structures have been noticed to appear from the surface. The in-situ formed urchin-like agglomerates were identified to comprise mostly out of Cu (Supplementary Fig. 16) and their formation was found to match well with the observed decrease in catalytic performance. Formation of such large structures is not possible through surface migration of copper atoms alone. Therefore, we hypothesize that there must have been a certain level of Cu dissolution and redeposition during CORR<sup>4</sup>. The observed reconstruction of the electrode's surface might originate from the change in the reaction environment when CO<sub>2</sub> is replaced with CO. Namely, our system with bicarbonate-based electrolyte and an AEM is well buffered during CO<sub>2</sub>RR, allowing for a continuous operation with a stable catholyte pH value between 8 and 9. However, when CO<sub>2</sub> is replaced with CO as the precursor gas, the buffer breaks at a certain time during operation, resulting in an increase in pH to values close to 14. Another reason for the decreased stability might be linked to the observed degradation of the anion-exchange membrane after exposure to high current densities and highly alkaline pH for a prolonged period of time. Finally, the formation of the urchin-like agglomerates was found to match well with the observed decrease in catalytic performance.



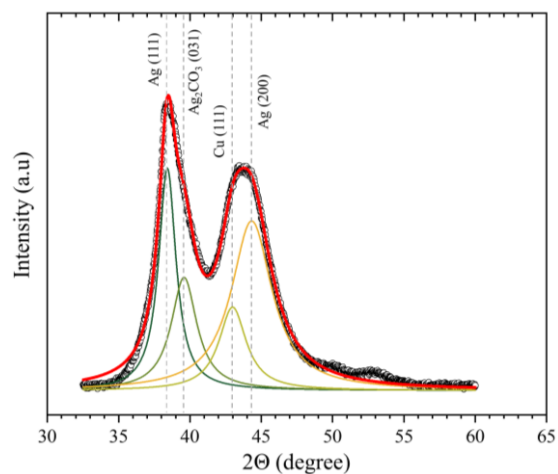
**Supplementary Figure 16.** SEM images showing (a) post-CORR and (b) post-CO<sub>2</sub>RR samples after being exposed to 300 mA cm<sup>-2</sup> for 7 h. Scale bar for both images is 3 μm.



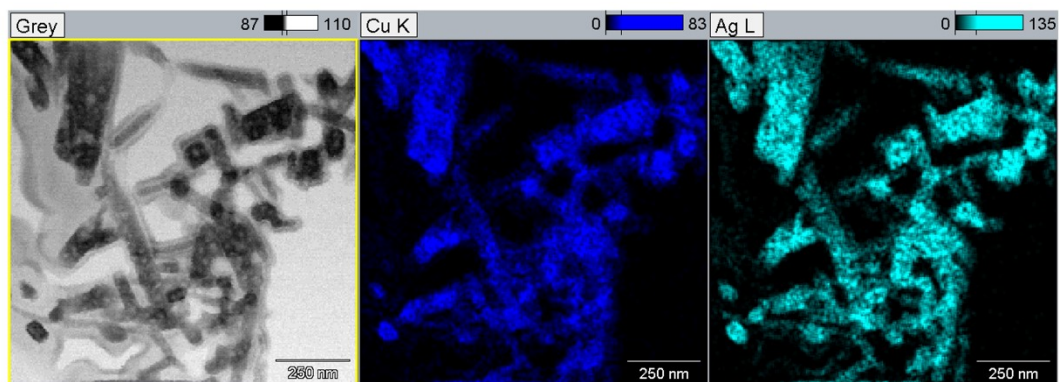
**Supplementary Figure 17.** EDX measurements performed on a post-electrolysis electrode sample which has been exposed to a constant current density of 300 mA cm<sup>-2</sup> for 7 h. The (a) SEM image shows the electrode's surface containing the urchin-like agglomerates. The position where the two EDX point scans were made are labeled with (b) a yellow and (c) a red dot.



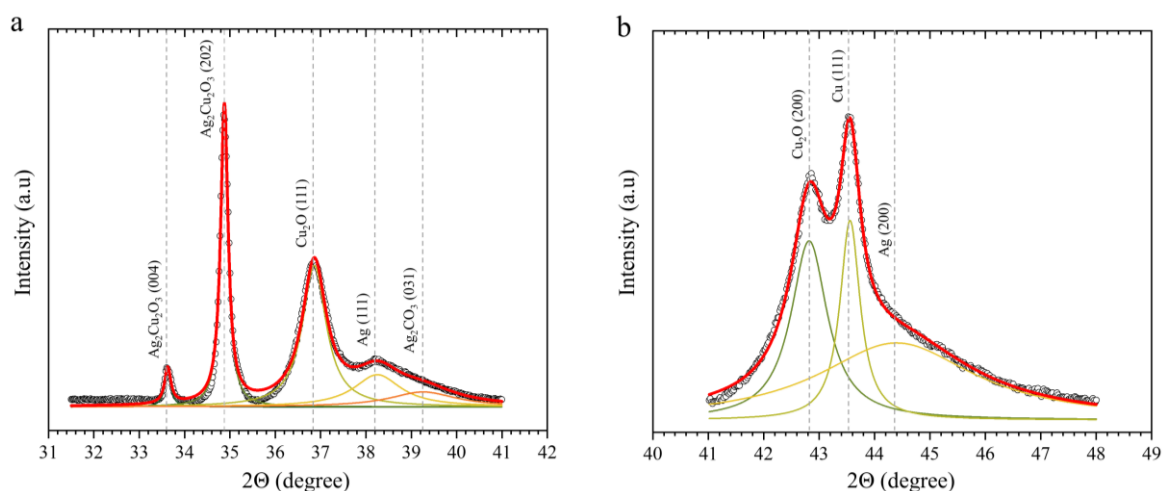
**Supplementary Figure 18.** (a) Exploded-view schematic of an EC-RTMS electrolytic cell used to detect hydrogen, methane and ethylene in real time shortly after the formation of the products on the electrode. The sandwich type cell consists of two compartments, one for the working electrode and another one for the counter electrode, separated by a proton conductive membrane. A reference electrode (BASi, West Lafayette, USA) is inserted from the side into the working electrode compartment. A deactivated fused silica glass capillary (Trajan Scientific Europe Ltd., Ringwood, Australia) hits on the working electrode under an angle of approximately 20° to extract electrolyte containing product species from the close proximity of the electrode. (b) Schematic of the EC-RTMS experimental set-up. The liquid stream coming out from the cathode chamber is forwarded to a custom-made degasser to separate the gas from the liquid electrolyte. The gases permeate through the wall of a tube membrane based on Teflon AF 2400 (Biogeneral, Inc., San Diego, USA) and are subsequently analyzed in an electron impact quadrupole mass spectrometer for real-time information.



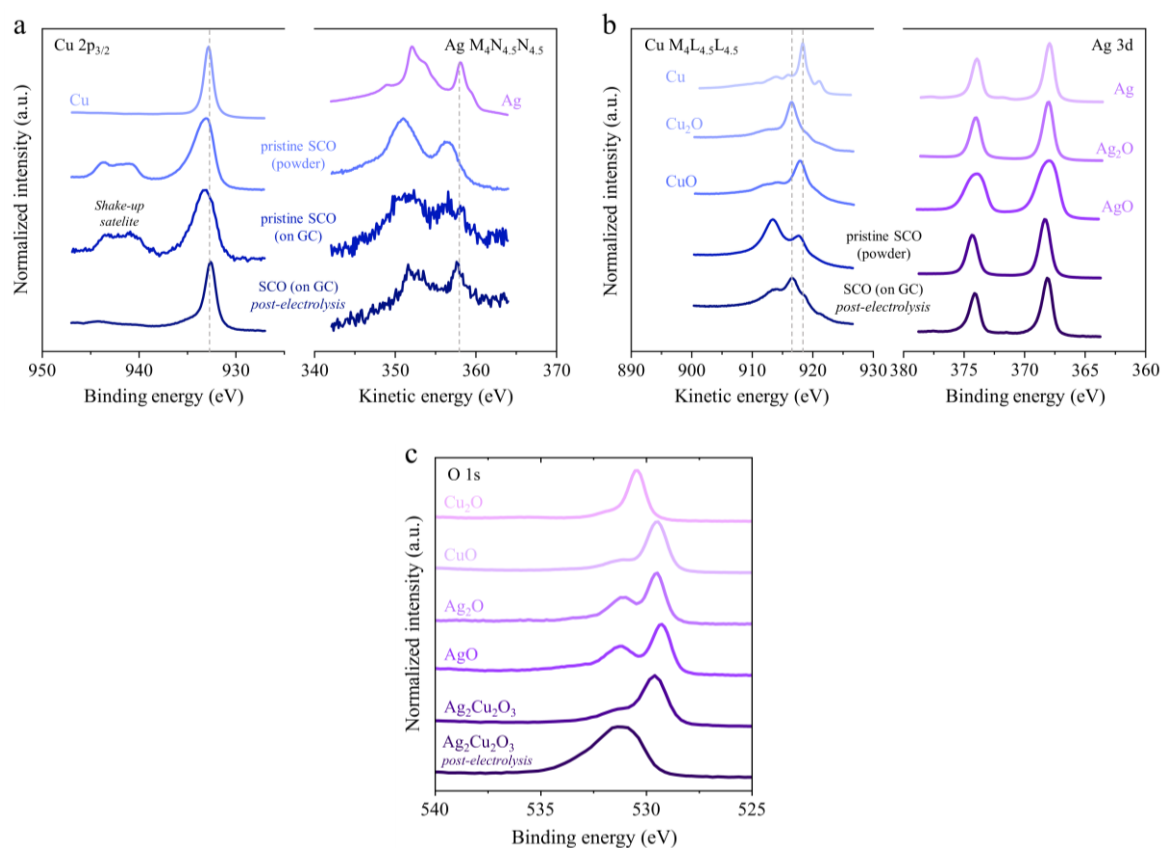
**Supplementary Figure 19.** Deconvoluted PXRD pattern of a sample which was exposed to a constant current density of  $40 \text{ mA cm}^{-2}$  under CO<sub>2</sub>RR conditions for 90 s. The full XRD pattern of this sample is shown in Fig. 4b of the original paper.



**Supplementary Figure 20.** Post-electrolysis STEM energy dispersive X-ray spectroscopy (EDX) elemental mapping of the catalyst material showing the distribution of elemental Cu and Ag within the particles.



**Supplementary Figure 21.** Deconvoluted PXRD patterns of a sample which was exposed to a constant current density of  $40 \text{ mA cm}^{-2}$  under  $\text{CO}_2\text{RR}$  conditions for 50 s.



**Supplementary Figure 22.** XPS spectra of (a) Cu  $2p_{3/2}$  and Ag MNN Auger regions and (b) Cu LMM Auger and Ag 3d regions for silver-copper oxide (and additional pristine reference samples) before and after electrolysis. The spectrum of Cu  $2p_{3/2}$  core level belonging to post electrolysis  $\text{Ag}_2\text{Cu}_2\text{O}_3$  (SCO – silver-copper oxide) sample does not possess a shake-up satellite peak which is clear indication of  $\text{Cu}^{2+}$  being present. The spectrum of the Cu LMM Auger region belonging to post electrolysis  $\text{Ag}_2\text{Cu}_2\text{O}_3$  sample shows presence of oxidized Cu species. Since post-electrolysis XRD measurements did not find any traces of oxide phases, the detected oxidized Cu can be attributed to the amorphous native oxide layer which formed on the surface of the sample due to the *ex-situ* nature of our XPS measurement. (c) XPS spectra of O 1s region for Cu and Ag oxide reference samples and  $\text{Ag}_2\text{Cu}_2\text{O}_3$  (pristine and post-electrolysis).

**Table** Error! No text of specified style in document..1. Interatomic distances and angles for Ag<sub>2</sub>Cu<sub>2</sub>O<sub>3</sub>, Ag<sub>2</sub>O and CuO based on previously reported crystallographic refinement <sup>5</sup>.

Bond (Å)	Ag <sub>2</sub> Cu <sub>2</sub> O <sub>3</sub>	Ag <sub>2</sub> O	CuO
Ag – O	2 x 2.073 4 x 3.480	2 x 2.061 6 x 3.912	-
Cu – O	2 x 1.906 2 x 1.988	-	2 x 1.955 2 x 1.957
Cu – Cu	2 x 2.943 4 x 3.387	-	4 x 2.900 4 x 3.082
Ag – Ag	2 x 2.943 4 x 3.387	3.366 4.760	-
Cu – Ag	2 x 2.943 4 x 3.387	-	-
O – O	2 x 2.470 4 x 2.940	4.122	2 x 2.626 2 x 2.896
Angle (°)	Ag <sub>2</sub> Cu <sub>2</sub> O <sub>3</sub>	Ag <sub>2</sub> O	CuO
O – Ag – O	180.0	180.0	-
O – Cu – O	79.9 100.1	-	84.3 95.7
Cu – O – Ag	116.6	-	-
Cu – O – Cu	104.7 116.8	-	84.3 95.4
Ag – O – Ag	90.4	109.5 58.5	-

**Table 2.** XPS data for Ag<sub>2</sub>Cu<sub>2</sub>O<sub>3</sub> (before and after electrolysis) and reference materials.

Sample	Ag 3d <sub>5/2</sub> (eV)	Ag MNN (eV)	α'-Ag (eV)	Cu 2p <sub>3/2</sub> (eV)	Cu LMM (eV)	F-parameter
Cu <sup>0</sup>	-	-	-	932.8	918.3	15.6
Cu <sub>2</sub> O	-	-	-	932.5	916.6	16.8
CuO	-	-	-	933.4	917.9	2.1
Ag <sup>0</sup>	368.0	358.1	726.1	-	-	-
Ag <sub>2</sub> O	368.0	356.2	724.2	-	-	-
AgO	367.9	356.7	724.6	-	-	-
Ag <sub>2</sub> Cu <sub>2</sub> O <sub>3</sub> <i>pristine</i>	368.3	356.5	724.8	933.1	917.6	2.7
Ag <sub>2</sub> Cu <sub>2</sub> O <sub>3</sub> <i>post-electrolysis</i>	368.1	357.6	725.7	932.6	916.6	8.1

**Table 2.** Current state-of-the-art catalysts for selective, high-rate ( $> 100 \text{ mA cm}^{-2}$ ) electrochemical reduction of CO to  $\text{C}_{2+}$  products.

<b><math>\text{C}_{2+}</math> Faradaic efficiency (%)</b>	<b><math>\text{C}_{2+}</math> partial current density (<math>\text{mA cm}^{-2}</math>)</b>	<b>Potential measured at the cathode (V vs RHE)</b>	<b>Electrolyte</b>	<b>Reference</b>
95	1188	-0.72	1M KOH	6
<b>93.5</b>	<b>467</b>	<b>-0.83</b>	<b>1M CsHCO<sub>3</sub></b>	<b>this work</b>
<b>91.7</b>	<b>550</b>	<b>-0.86</b>	<b>1M CsHCO<sub>3</sub></b>	<b>this work</b>
91	635	-0.67	2M KOH	7
89	341	-0.66	1M KOH	8
83	145	-0.66	1M KOH	9
70	124	-0.96	0.1M KOH	10
69	138	-0.74	2M KOH	11
64	70	-0.96	1M KOH	12

## References:

- 1 L. Debbichi, M. C. Marco De Lucas, J. F. Pierson and P. Krüger, *J. Phys. Chem. C*, 2012, **116**, 10232–10237.
- 2 A. P. Litvinchuk, A. Möller, L. Debbichi, P. Krüger, M. N. Iliev and M. M. Gospodinov, *J. Phys. Condens. Matter*, 2013, **25**, 105402.
- 3 C. W. Li, J. Ciston and M. W. Kanan, *Nature*, 2014, **508**, 504–507.
- 4 F. D. Speck and S. Cherevko, *Electrochem. commun.*, 2020, **115**, 106739.
- 5 D. Muñoz-Rojas, G. Subías, J. Fraxedas, P. Gómez-Romero and N. Casañ-Pastor, *J. Phys. Chem. B*, 2005, **109**, 6193–6203.
- 6 J. Li, Z. Wang, C. McCallum, Y. Xu, F. Li, Y. Wang, C. M. Gabardo, C. T. Dinh, T. T. Zhuang, L. Wang, J. Y. Howe, Y. Ren, E. H. Sargent and D. Sinton, *Nat. Catal.*, 2019, **2**, 1124–1131.
- 7 M. Jouny, W. Luc and F. Jiao, *Nat. Catal.*, 2018, **1**, 748–755.
- 8 J. Li, F. Che, Y. Pang, C. Zou, J. Y. Howe, T. Burdyny, J. P. Edwards, Y. Wang, F. Li, Z. Wang, P. De Luna, C. T. Dinh, T. T. Zhuang, M. I. Saidaminov, S. Cheng, T. Wu, Y. Z. Finfrock, L. Ma, S. H. Hsieh, Y. S. Liu, G. A. Botton, W. F. Pong, X. Du, J. Guo, T. K. Sham, E. H. Sargent and D. Sinton, *Nat. Commun.*, 2018, **9**, 1–9.
- 9 Y. Pang, J. Li, Z. Wang, C. S. Tan, P. L. Hsieh, T. T. Zhuang, Z. Q. Liang, C. Zou, X. Wang, P. De Luna, J. P. Edwards, Y. Xu, F. Li, C. T. Dinh, M. Zhong, Y. Lou, D. Wu, L. J. Chen, E. H. Sargent and D. Sinton, *Nat. Catal.*, 2019, **2**, 251–258.
- 10 J. Li, K. Chang, H. Zhang, M. He, W. A. Goddard, J. G. Chen, M. J. Cheng and Q. Lu, *ACS Catal.*, 2019, **9**, 4709–4718.
- 11 W. Luc, X. Fu, J. Shi, J. J. Lv, M. Jouny, B. H. Ko, Y. Xu, Q. Tu, X. Hu, J. Wu, Q. Yue, Y. Liu, F. Jiao and Y. Kang, *Nat. Catal.*, 2019, **2**, 423–430.
- 12 T.-T. Zhuang, Y. Pang, Z.-Q. Liang, Z. Wang, Y. Li, C.-S. Tan, J. Li, C. T. Dinh, P. De Luna, P.-L. Hsieh, T. Burdyny, H.-H. Li, M. Liu, Y. Wang, F. Li, A. Proppe, A. Johnston, D.-H. Nam, Z.-Y. Wu, Y.-R. Zheng, A. H. Ip, H. Tan, L.-J. Chen, S.-H. Yu, S. O. Kelley, D. Sinton and E. H. Sargent, *Nat. Catal.*, 2018, **1**, 946–951.